

Article

Method for Reconstructing Velocity Field Images of the Internal Structures of Bridges Based on Group Sparsity

Jian Li ^{1,*}, Jin Li ¹, Chenli Guo ¹, Hongtao Wu ², Chuankun Li ¹, Rui Liu ¹ and Lujun Wei ¹

¹ Shanxi Key Laboratory of Intelligent Detection Technology & Equipment, North University of China, Taiyuan 030051, China; sz202205003@st.nuc.edu.cn (J.L.)

² Shanxi Intelligent Transportation Laboratory Co., Ltd., Taiyuan 030032, China

* Correspondence: lijian@nuc.edu.cn

Abstract: Non-destructive testing (NDT) enables the determination of internal defects and flaws in concrete structures without damaging them, making it a common application in current bridge concrete inspections. However, due to the complexity of the internal structure of this type of concrete, limitations regarding measurement point placement, and the extensive detection area, accurate defect detection cannot be guaranteed. This paper proposes a method that combines the Simultaneous Algebraic Reconstruction Technique with Group Sparsity Regularization (SART-GSR) to achieve tomographic imaging of bridge concrete under sparse measurement conditions. Firstly, a mathematical model is established based on the principles of the tomographic imaging of bridge concrete; secondly, the SART algorithm is used to solve for its velocity values; thirdly, on the basis of the SART results, GSR is applied for optimized solution processing; finally, simulation experiments are conducted to verify the reconstruction effects of the SART-GSR algorithm compared with those of the SART and ART algorithms. The results show that the SART-GSR algorithm reduced the relative error to 1.5% and the root mean square error to 89.76 m/s compared to the SART and ART algorithms. This improvement in accuracy makes it valuable for the tomographic imaging of bridge concrete and provides a reference for defect detection in bridge concrete.

Keywords: non-destructive testing; travel time tomography; bridge concrete; joint iterative reconstruction algorithm; group sparsity; dictionary learning



Citation: Li, J.; Li, J.; Guo, C.; Wu, H.; Li, C.; Liu, R.; Wei, L. Method for Reconstructing Velocity Field Images of the Internal Structures of Bridges Based on Group Sparsity. *Electronics* **2024**, *13*, 4574. <https://doi.org/10.3390/electronics13224574>

Academic Editor: Silvia Liberata Ullo

Received: 19 September 2024

Revised: 11 November 2024

Accepted: 13 November 2024

Published: 20 November 2024



Copyright: © 2024 by the authors. Licensee MDPI, Basel, Switzerland. This article is an open access article distributed under the terms and conditions of the Creative Commons Attribution (CC BY) license (<https://creativecommons.org/licenses/by/4.0/>).

1. Introduction

The continuous growth in the number of bridges has led to increasingly severe issues relating to bridge problems. To address the problem of detecting the quality of bridge concrete, research on new bridge acoustic tomography imaging technology for bridge concrete structures has been conducted. These studies present innovative approaches that address the gap in detecting the internal structures of concrete bridges. Their application is crucial for enhancing the quality and durability of bridges during construction. Currently, the methods for detecting internal defects in concrete structures mainly include the ultrasonic pulse method, radar-scanning method, impact-echo method, and infrared imaging method. Numerous scholars at home and abroad have studied these methods. Bond et al. have used travel time tomography to detect cracks in large volumes of dam concrete. Vassilios K Karastathis [1] applied acoustic tomography technology to assess the quality of concrete in the Marathon Dam. Nandipati S M Ravi Kumar [2] et al. have used ultrasonic technology to evaluate the uniformity of concrete and reveal defects. Alexey Tatarinov [3] et al. have developed an ultrasonic testing method to monitor the development of railway sleeper cracks. Monika Zielińska [4] et al. have proposed a theoretical model combined with CT scanning to determine the propagation paths of elastic waves in reinforced concrete. Thiele Marc [5]. et al. applied acoustic measurements to study the fatigue process of concrete and found that ultrasonic measurements could identify damage characteristics caused by

loading. Donda Dipesh P [6] et al. have used ground-penetrating radar (GPR) technology to detect defects and rebar in concrete under laboratory conditions. Singh Sanjeev K [7] et al. adopted millimeter-wave evaluation methods to non-destructively test the damage inflicted on concrete structures after a fire, and compared with ultrasonic pulse velocity technology, they found consistent results between the two. Ma Ye [8] et al. have developed a method using geological radar to detect moisture-related damage in asphalt pavements, introducing the “Accumulated Intralayer Peak” (AIP) index to detect spalling damage. Jin Hui [9] et al. have studied the feasibility of using infrared thermography to detect internal voids in concrete bridges. Brigitte Goffin [10] et al. have used infrared thermography technology to study the effect of the corrosion of epoxy-coated and uncoated steel bars in concrete on thermal behavior. Sam Ang Keo [11] et al. have explored the application of microwave infrared thermography technology in detecting defects in carbon-fiber-reinforced polymer-composite-material-reinforced concrete specimens. Abd Wahid Rasib [12] et al. used thermal imaging sensors carried by drones to inspect surface defects in concrete on bridge columns, successfully identifying surface defects. Scherr Johannes F [13] et al. used an impact-echo scanner to perform delamination detection on large areas of concrete bridge decks, determining repair needs and checking repair effects. Liu Yun Lin [14] et al. have conducted experimental and numerical studies to detect debonding defects in the grouting layer of precast concrete components using the impact-echo method. Hu Xinmin [15] et al. have proposed a multi-parameter comprehensive interpretation method based on impact elastic waves for the rapid detection of internal defects in hydraulic tunnel linings. Li Hongyan [16] et al. compared the reconstruction effects of iterative algorithms such as the Algebraic Reconstruction Technique (ART) and the Simultaneous Algebraic Reconstruction Technique (SART) and, based on this, developed an improved algebraic reconstruction method. They calculated two consecutive results using the algebraic reconstruction algorithm and then used the weighted sum of these two results to correct the reconstructed image, obtaining iterative results and reducing noise.

However, due to high experimental costs, the testing conditions for large-scale bridge concrete structures cannot guarantee a dense distribution of sensor measurement points, and data collection is prone to errors. Therefore, the imaging accuracy is not ideal, which is a problem awaiting resolution. To address the above issues, in this paper, we propose a combination of the Simultaneous Algebraic Reconstruction Technique (SART) and the Group-Sparsity Regularization (GSR) method. The application of group sparsity technology provides new possibilities for improving image reconstruction accuracy and efficiency. By utilizing the characteristics of internal defects in concrete and their structural properties, group-sparsity-derived prior knowledge can handle incomplete or noise-corrupted observation data, accurately recover the original signal, and facilitate more precise and stable image reconstruction.

2. Related Work

Nandipati S M Ravi Kumar et al. evaluated the uniformity of concrete structures by using ultrasonic pulse velocity testing and contour-mapping techniques. The contour maps generated from ultrasonic pulse velocity values displayed the level of structural uniformity. The color variations in the contour maps revealed defects present in the structure. This interpretation strategy provided an appropriate tool for the assessment of concrete structures. Alexey Tatarinov et al. developed a method in which ultrasonic testing is used to monitor and quantify transverse and longitudinal cracks in railway prestressed concrete sleepers. By analyzing the time and energy parameters of ultrasonic signals, this method was successfully used to evaluate the fast and slow components of ultrasonic propagation to monitor the depth development and temporal changes of cracks. Field studies conducted on Latvian railways verified the effectiveness of this method through comparative tests on healthy and cracked sleepers. The research results indicate that as cracks gradually expand, the propagated ultrasonic signal attenuates, and the ratio of slow-to-fast wave components tilts towards the slow waves. Combining these two manifestations

can provide quantitative indicators of the cracking process. Monika Zielińska M et al. developed a new theoretical model to determine the propagation paths of elastic waves in reinforced concrete structures, including transmission, refraction, reflection, and creeping waves along the surface of inclusions. Wave propagation measurements were performed on the surfaces of beams and computerized tomography scanning was conducted to image the internal structures of the test beams. Ray tracing was employed via a hybrid method combining network theory with ray-bending methods. The research results show that ultrasonic tomography has great potential in detecting debonding in reinforced concrete structures. Thiele Marc et al. employed acoustic measurement techniques to investigate the fatigue process of concrete under compressive cyclic loading. In addition to acoustic emission and ultrasonic signal measurements, they incorporated other non-destructive testing methods, including strain, elastic modulus, and static strength measurements. Their research revealed that ultrasonic measurements could determine the anisotropic characteristics of fatigue damage caused by uniaxial loading. Additionally, it was observed that fatigue damage does not seem to be entirely composed of crack structures parallel to the load direction; crack structures perpendicular to the load and local compaction may also be components of fatigue damage. However, the aforementioned methods do not consider the limitations of defect detection in large bridge structures and are unable to guarantee the detection accuracy of large structural concrete. For instance, for long-span suspension bridges or cable-stayed bridges, due to their complex dynamic characteristics and large scale, the ultrasonic pulse method may struggle to accurately capture all the important modal information.

Donda Dipesh P et al. used ground-penetrating radar (GPR) technology in a laboratory environment to study signal attenuation by simulating concrete slabs under different depth and material conditions to detect surface and subsurface defects and rebar in concrete. Their research revealed that the reflection amplitudes of different materials at varying depths show significant changes, which is helpful for the detection and standardized quantification of subsurface cracks in actual structures such as concrete bridge decks, providing decision makers with useful information for monitoring and planning structural repairs and reinforcement. Singh Sanjeev K et al. introduced a novel millimeter-wave evaluation method as a non-destructive test for assessing fire damage in concrete civil engineering structures. They utilized an active millimeter-wave radar system operated at 55–65 GHz to measure the complex relative permittivity of concrete cube specimens. The results were compared with those obtained using the existing ultrasonic pulse velocity technique, revealing good consistency between the two methods. Ma Ye et al. developed a method in which ground-penetrating radar (GPR) is used to detect moisture-related spalling damage in asphalt pavements. A finite-difference time-domain-based simulation program was used to study the propagation of GPR signals in damaged pavements, and a new GPR indicator, “Accumulated Intralayer Peak” (AIP), was introduced to detect spalling damage in asphalt pavements. Field data and visual inspection of pavement cores were used to verify the effectiveness of this indicator and assess its performance in detecting the presence, extent, and severity of spalling in sections of pavement in use. Their study found that voids in the middle of the AC layer produce positive peaks in the reflected waves, while intermediate peaks at the interface between the AC layer and the base layer are related to spalling damage in the AC layer. The AIP had accuracy rates of 80% for predicting spalling and 96% for predicting non-spalling sections, demonstrating its effectiveness in detecting spalling damage in flexible pavements. The above methods, when applied to actual defect detection in bridge concrete, can be affected by reinforcing-bar reflection signals, leading to masking or confusion of defect signals. For example, during the inspection of a certain bridge, some anomalous signals were detected using ground-penetrating radar (GPR). Upon careful analysis, it was found that these anomalies did not originate from defects within the concrete itself but rather from irregular arrangements or corrosion of the reinforcing steel.

Jin Hui et al. explored the application of infrared thermography in detecting internal voids and other structural issues in concrete bridges. They analyzed the relationship between concealed structural issues in concrete bridges and infrared thermograms at the theoretical level and verified the feasibility of using infrared thermography to detect internal defects in bridge concrete by establishing a concrete model containing inner = cavity defects and conducting finite element simulation analysis. The final finite element simulation results coincided with those from theoretical analysis, indicating that it is feasible to use infrared thermography technology to detect internal defects in bridge concrete. Brigitte Goffin et al. studied the effect of corrosion on the thermal behavior of reinforced concrete without electromagnetic influence using infrared thermography technology in order to detect epoxy-coated and uncoated steel reinforcement. By inserting heating elements into the steel reinforcement embedded in the concrete and heating the steel from the inside, the thermal response of the concrete surface was monitored using an infrared camera. The thermal measurement results showed that corrosion thermally isolated the uncoated steel reinforcement, while the corrosion of epoxy-coated steel reinforcement caused the coating to crack, thereby reducing the thermal isolation effect of the steel. Sam Ang Keo et al. studied the application of microwave infrared thermography technology in detecting and characterizing defects in carbon-fiber-reinforced polymer-composite-material-reinforced concrete specimens. A numerical model including a broadband pyramid horn antenna and specimens was constructed, and two operating modes were experimentally validated using a 360-watt power system. The study found that MIRT has the potential to become a method for identifying defects in CFRP-strengthened concrete structures. Wahid Rasib et al. utilized thermal imaging sensors mounted on drones to inspect surface defects in concrete bridge columns, successfully identifying surface defects through close-range remote sensing NDT and image segmentation analysis. However, the above methods do not consider the impact of external environmental conditions on the detection results during the actual infrared thermography technology detection process. Taking the quality inspection of an exterior wall finish on a high-rise building as an example, when using infrared thermography for the inspection, it was found that due to strong sunlight and high wind speeds on the day of the inspection, the temperature distribution on the exterior wall surface was uneven, leading to some misjudgments. After multiple repeated inspections and adjusting the timing of the inspections (choosing cloudy days or evenings), more accurate results were finally obtained.

Scherr Johannes F et al. conducted a large-scale on-site study using a prototype impact-echo scanner on a concrete bridge deck with a total area of over 17,000 square meters to detect delaminations. Manual tapping and coring confirmed the presence of delaminations in known sections of the bridge. An extensive damage assessment helped determine the need for repair work. Based on the preliminary results, two lanes of the bridge were repaired, and the bond between new and old concrete was examined in subsequent tests. Liu Yun Lin et al. performed experimental and numerical studies on the grout layer between precast concrete components in assembly structures, aiming to detect interface-debonding defects based on impact-echo theory. Their study tested the impact-echo method under two different boundary conditions. The results showed that thickness frequencies near free boundaries were significantly lower than those near fixed boundaries. Additionally, boundary effects disappeared when the impact location was sufficiently far from any boundaries. These characteristics can be used to identify debonding layers in grout joints (i.e., near free boundaries). Additionally, blind on-site tests were conducted to verify the effectiveness of the proposed impact-echo method in detecting debonding layers. Hu Xinmin et al. introduced a multi-parameter comprehensive interpretation method based on impact elastic waves for the rapid detection of internal defects in hydraulic tunnel linings. This method combines common time offset domain analysis, frequency domain analysis, and two-dimensional Rayleigh wave methods for data processing. The aforementioned detection method involves single data acquisition and multi-parameter joint interpretation. Concrete lining tests were conducted on physical models and compared

with results obtained using the ground-penetrating radar method to validate the accuracy of the method. Coring results demonstrated the reliability and stability of the method in practical applications. Compared to ultrasonic pulse methods, radar scanning, and infrared imaging, the impact-echo method shows clear advantages in terms of operational simplicity, testing speed, cost-effectiveness, and applicability for defect detection in bridge concrete. However, its imaging precision still needs improvement due to limitations in the number of measurement points.

3. Construction of Travel-Time Tomography Model

The impact of the excitation hammer on the ground produces spherical surface wave signals that propagate along straight rays (the normal family of wave fronts). The travel time of elastic waves during transmission is determined by their speed and geometric paths. The time it takes the elastic waves to reach the sensor array is known as the travel time, which is a function of both the velocity and path.

$$t = \int_L \frac{1}{v} dr = \int_L S dr \tag{1}$$

Among the variables above, t represents the travel time; v represents the velocity of shockwave propagation; s represents the slowness; L is the ray path; and dr indicates a segment of the ray path.

The test area is divided into several regular or irregular grid cells, as shown in Figure 1. The equation mentioned above is discretized, and for the i -th ray,

$$t_i = \sum_{j=1}^N a_{ij} s_j, i = 1, 2, \dots, I, j = 1, 2, \dots, J \tag{2}$$

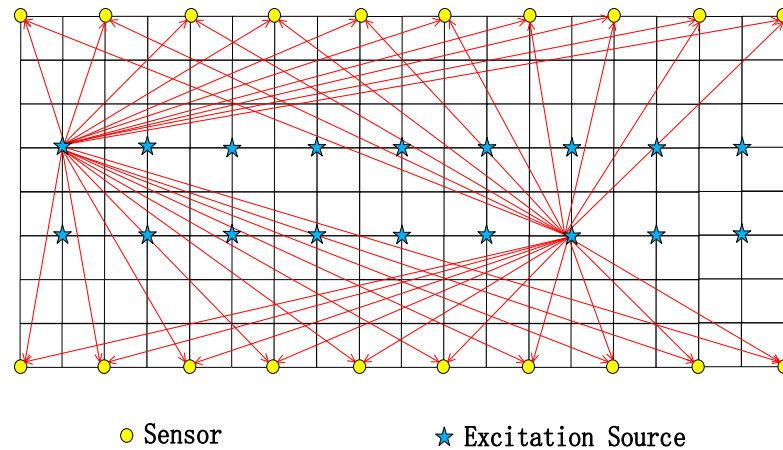


Figure 1. Sketch of the travel-time tomography model.

In the equation given above, t_i represents the I -dimensional vector of travel times for the i -th ray from the seismic source to the sensor; s_j denotes the slowness value of the j -th grid; a_{ij} represents the coefficient projection of the i -th ray passing through the j -th grid, and it is a matrix with dimensions of $I \times J$; I is the number of rays, which is the product of the number of activation points and the number of sensors; and J is the number of grids. The equation, written in matrix form, is

$$AS = T \tag{3}$$

Here, $T = (t_1, t_2 \dots t_I)'$ is the M -dimensional column vector of travel times for each ray; $S = (s_1, s_2 \dots s_J)'$ is the slowness value of discrete units, which is the reciprocal of wave speed and an N -dimensional column vector; and A is a matrix of the order of $I \times J$.

This paper is primarily concerned with solving Equation (3) to determine the value of S . In the equation mentioned above, the elements of matrix T represent the travel times of rays passing through the grids, which are related to the length of the propagation ray passing through the grids between the stimulation point and the sensor. Not all grids are traversed by rays; therefore, Equation (3) constitutes a large system of underdetermined equations.

4. Methods for Solving the Tomographic Imaging Model of Internal Structural Velocity Field in Bridges

4.1. Simultaneous Algebraic Reconstruction Technique

In the process of actual bridge concrete wave velocity inversion reconstruction, due to the sparse sensor measurement points and the limited quantity of data obtained, the analytical equation set for bridge concrete is a large underdetermined system of equations, making it difficult for traditional solution methods to obtain more precise solutions. To address the issue of underdetermined systems of equations, a series of inversion algorithms have emerged, including the Back Projection Technique [17] (BPT), the Algebraic Reconstruction Technique [18] (ART), the Simultaneous Iterative Reconstruction Technique (SIRT), and the Simultaneous Algebraic Reconstruction Technique (SART).

The Algebraic Reconstruction Technique (ART) is a relatively old iterative reconstruction algorithm proposed by R. Gordon and others that has been widely used in image reconstruction. Compared to analytical reconstruction methods, iterative methods offer significant advantages, as they can yield good reconstruction results even when some projection data are missing. The iterative steps of the ART method involve correcting each ray in each image sequentially, which not only requires a large amount of computation but also poses issues regarding slow convergence and potential non-convergence. Equation (4) represents the iterative formula for the ART algorithm:

$$s_j^{k+1} = s_j^k + \lambda \frac{a_{ij}}{\sum_{j=1}^J a_{ij}^2} \left(t_i - \sum_{j=1}^J a_{ij} s_j^k \right) \quad (4)$$

Here, s_j^k is the slowness of the j -th grid after k iterations; t_i is the actual measured projection value; a_{ij} is the projection coefficient, that is, the length of the i -th ray in the j -th grid; λ is the relaxation factor, usually in the range of $(0, 2)$; and k is the number of iterations.

The Simultaneous Algebraic Reconstruction Technique [19] (SART) is an iterative reconstruction algorithm that combines the advantages of both the ART and SIRT. Unlike the ART, which updates only the pixels affected by a single ray in each iteration, the SART considers the information from all rays within a projection view to update the pixels. This helps reduce image noise and improve reconstruction quality. Compared to the SIRT, the SART maintains a similar noise suppression ratio but enhances the convergence speed of the algorithm, making it more suitable for handling large-scale problems. The basic idea behind the SART algorithm is to calculate the projection error for all rays at each projection angle and then update each pixel in the image. This effectively reduces the noise introduced by the ART algorithm, as shown in Equation (5):

$$s_j^{k+1} = s_j^k + \frac{\lambda}{\sum_{j=1}^J a_{ij}} \cdot \sum_{j=1}^J \frac{a_{ij} \cdot \left(t_i - \sum_{j=1}^J a_{ij} s_j^k \right)}{\sum_{j=1}^J a_{ij}} \quad (5)$$

Here, s_j^k is the slowness of the j -th grid after k iterations; t_i is the actual measured projection value; a_{ij} is the projection coefficient, that is, the length of the i -th ray in the j -th grid; λ is the relaxation factor, usually in the range of $(0, 2)$; k is the number of iterations; and I is the projection collection.

4.2. Group Sparse Modeling

Sparsity has become an important characteristic of natural images, and regularization techniques for sparsity are widely used in image-processing methods such as denoising, image restoration [20], and resolution enhancement. Sparse models assume that every pixel in an image can be represented by elements in a dictionary, which are extracted from natural images by taking image patches and training them.

Group sparsity is an optimization technique [21] that extends the sparsity constraint from individual elements to groups of elements, operating at the group level. This extension allows algorithms to effectively maintain relationships between elements within a group while achieving a more effective sparse representation in complex scenarios [22]. In group sparsity, the non-local self-similarity principle is used to find image blocks with similar structures [23], thereby further enhancing the effectiveness of sparse representation.

Feature extraction is a key step [24] that determines the quality of subsequent processing. To effectively describe and classify image textures, it is necessary to identify more indicators that reflect image characteristics and extract these features through analysis and transformation. Traditional block-sparsity-based methods typically divide images into multiple overlapping small blocks and process them separately, but this can result in a loss of similarity between blocks, leading to inaccurate sparsity coefficients. Therefore, this paper proposes a new method that does not process image blocks in a fixed order but rather clusters similar blocks together to form a group-based sparse representation. This approach considers both sparsity and non-local similarity in images, allowing for adaptive handling of image sparsity within the group domain. Figure 2 is a schematic of how the group sparsity method is employed in image reconstruction.

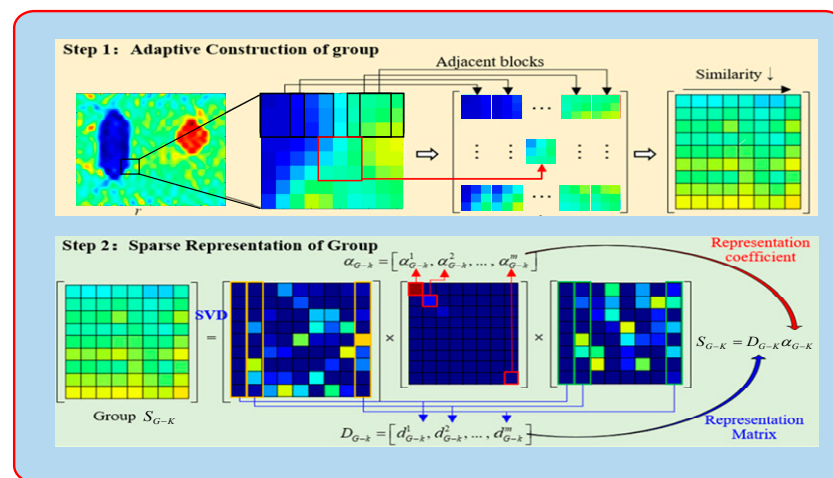


Figure 2. Adaptive group sparsity image reconstruction.

The specific steps are as follows: Divide the bridge concrete slowness distribution S with a size of X into n regions S_k ($k = 1, 2, \dots, n$) with dimensions of $\sqrt{B_X} \times \sqrt{B_X}$. For each region S_k , use the Structure Similarity Index Measure (SSIM), denoted as $SSIM(S_k, S_i) \geq \zeta$, as the metric for assessing the similarity between wave velocity regions. ζ is a preset threshold value. Within an $L \times L$ search window, select c blocks that are most similar to the region block q_k . The Structure Similarity Index is defined as

$$SSIM(x, y) = \frac{(2\mu_x\mu_y + C_1)(2\sigma_{xy} + C_2)}{(\mu_x^2 + \mu_y^2 + C_1)(\sigma_x^2 + \sigma_y^2 + C_2)} \tag{6}$$

where μ_x and μ_y are the mean values of each block, which are used as estimated values, σ_x and σ_y are the standard deviations of each block, used as contrast estimation values. The higher the SSIM value, the more similar the values of x and y .

Translate the blocks into column vectors, and then arrange the c regions found in matrix form, denoted as S_{G_k} ($S_{G_k} = \{S_{G_k \times 1}, S_{G_k \times 2}, \dots, S_{G_k \times c}\}$). This matrix is referred to as the similar block group, as defined by Equation (7).

$$S_{G_k} = H_{G_k}(S) \tag{7}$$

Here, $H_{G_k}(\cdot)$ is the S_{G_k} operator extracted from S , and $H_{G_k}^T(\cdot)$ is the transposition of $H_{G_k}(\cdot)$. Transposing it allows each group S_{G_k} to be placed back into the corresponding k position in the reconstructed image, with the other positions being equal to zero. To obtain the slowness values for the entire detection area, average all the groups yielding, Equation (8).

$$S = \frac{\sum_{k=1}^n H_{G_k}^T(S_{G_k})}{\sum_{k=1}^n H_{G_k}^T(1_{B_S \times c})} \tag{8}$$

where $1_{B_S \times c}$ is a matrix of the same size as S_{G_k} , filled with ones.

According to the above definition, it can be clearly seen that each image block S_k corresponds to a group S_{G_k} . It can also be seen in Figure 3 that the construction of S_{G_k} clearly involves the utilization of the self-similarity of the image.

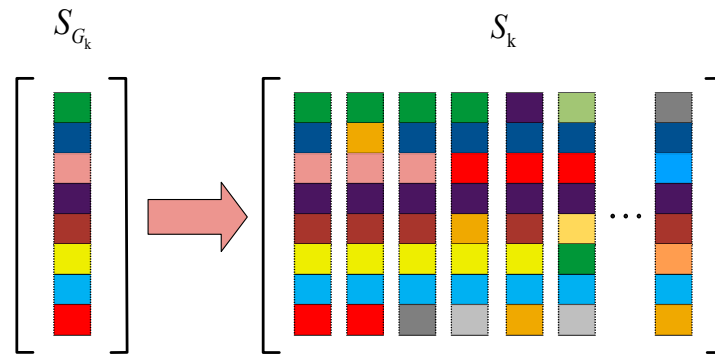


Figure 3. Construction of similar block groups.

Due to various factors affecting the signals received during actual measurement, it is not possible to directly determine the values of S and S_{G_k} from the signals obtained. Therefore, an estimate m_{G_k} of S_{G_k} is used for dictionary learning. Singular Value Decomposition (SVD) is then applied to m_{G_k} , resulting in Equation (9).

$$m_{G_k} = U_{G_k} \Sigma_{G_k} V_{G_k}^T = \sum_{i=1}^r \eta_{m_{G_k \times i}} (u_{G_k \times i} v_{G_k \times i}^T) \tag{9}$$

where r is the number of atoms in D_{G_k} : $\eta_{m_{G_k}} = \{\eta_{m_{G_k \times 1}}, \eta_{m_{G_k \times 2}}, \dots, \eta_{m_{G_k \times r}}\}$; $\Sigma_{G_k} = \text{diag} \eta_{m_{G_k}}$ is a diagonal matrix with all elements off the main diagonal being zero; $u_{G_k \times i}$ is a column of U_{G_k} ; and $v_{G_k \times i}^T$ is a column of V_{G_k} . For each group, the definition of each atom in D_{G_k} is given by Equation (10).

$$d_{G_k \times i} = u_{G_k \times i} v_{G_k \times i}^T \tag{10}$$

Finally, we define the corresponding adaptive dictionary D_{G_k} for each group, as expressed in Equation (11).

$$D_{G_k} = \{d_{G_k \times 1}, d_{G_k \times 2}, \dots, d_{G_k \times r}\} \tag{11}$$

In practical applications, the sparse representation model is defined as

$$\alpha = \operatorname{argmin}_{\alpha} \frac{1}{2} \|T - AS\|_2^2 + \lambda \|\alpha\|_1 \tag{12}$$

In the aforementioned formula, the first term is the data fidelity term, and the second term is the regularization term. The role of the regularization parameter λ is to control the degree of sparse representation. The GSR model represents the slowness S of the entire detection area by using the dictionary D_{G_k} to find sparse coefficients $\alpha_{G_k \times i}$

$$S = D_G \alpha_G = \frac{\sum_{k=1}^n H_{G_k}^T (\sum_{i=1}^r \alpha_{G_k \times i} d_{G_k \times i})}{\sum_{k=1}^n H_{G_k} (1_{B_X \times c})} \tag{13}$$

where D_G is the merging of D_{G_k} , and α_G is the merging of α_{G_k} .

Therefore, the GSR model corresponds to

$$\alpha_G = \operatorname{argmin}_{\alpha_G} \frac{1}{2} \|T - AS\|_2^2 + \lambda \|\alpha_G\|_1 \tag{14}$$

Upon comparing Equation (12) with Equation (14), it is evident that the primary difference between them lies in the units used for dictionary learning and sparse representation. In Equation (14), the GSR model employs groups as the basic units for sparse representation, which are formed by similar patches found within a search window. Therefore, during the process of dictionary learning and sparse coding, not only is the local sparsity of slowness distribution utilized but also its non-local similarity, leading to better slowness reconstruction results. Moreover, Equation (14) introduces adaptive dictionary learning for each group instead of learning a general dictionary for all patches, which not only reduces the complexity of learning but also facilitates large-scale optimization.

4.3. SART Algorithm Based on Group Sparsity Regularization

The SART-GSR algorithm primarily consists of two steps: The first step involves using the SART (Simultaneous Algebraic Reconstruction Technique) algorithm to solve Equation (3), resulting in solution \hat{S} . The second step involves the use of \hat{S} as the initial value and the use of GSR (Graduated Non-Convexity for Sparse Reconstruction) to reduce artifacts in \hat{S} , leading to solution S via the optimization of Equation (14). This is equivalent to

$$\min_{\alpha_G, S} \frac{1}{2} \|S - \hat{S}\|_2^2 + \lambda \|\alpha_G\|_1, \text{ X.t. } S = D_G \alpha_G \tag{15}$$

Since Equation (15) is a combinatorial optimization problem, it cannot be solved directly. This paper adopts the Iterative Soft Thresholding (IST) algorithm to iteratively optimize Equation (15). The iteration process is as follows:

$$m^t = S^t - \delta(S^t - \hat{S}) \tag{16}$$

$$S^{t+1} = \operatorname{argmin}_{\alpha_G} \frac{1}{2} \|S - m^t\|_2^2 + \lambda \|\alpha_G\|_1 \tag{17}$$

where δ is a constant and t represents the number of iterations. In each iteration, the following equation holds [23]:

$$\frac{1}{X} \|S^t - m^t\|_2^2 = \frac{1}{K} \sum_{k=1}^n \|x_{G_k} - m_{G_k}\|_F^2 \tag{18}$$

where $K = B_X \times c \times n$. Substituting Equation (18) into Equation (17) yields Equation (19).

$$\min_{\alpha_G} \sum_{k=1}^n \left(\frac{1}{2} \|S_{G_k} - m_{G_k}\|_F^2 + \tau \|\alpha_{G_k}\|_1 \right) \tag{19}$$

where $\tau = \lambda K/X$. Equation (19) is equivalent to several subproblems:

$$\operatorname{argmin}_{\alpha_{G_k}} \frac{1}{2} \| S_{G_k} - m_{G_k} \|_F^2 + \tau \| \alpha_{G_k} \|_1 \tag{20}$$

In Equation (20), since $S_{G_k} = D_{G_k} \alpha_{G_k}$ and $m_{G_k} = D_{G_k} \eta_{m_{G_k}}$, and due to the unitary invariance of dictionary D_{G_k} , it follows that

$$\| D_{G_k} \alpha_{G_k} - D_{G_k} \eta_{m_{G_k}} \|_F^2 = \| \alpha_{G_k} - \eta_{m_{G_k}} \|_2^2 \tag{21}$$

Therefore, Equation (20) can also be written as

$$\operatorname{argmin}_{\alpha_{G_k}} \frac{1}{2} \| \alpha_{G_k} - \eta_{m_{G_k}} \|_2^2 + \tau \| \alpha_{G_k} \|_1 \tag{22}$$

Therefore, the approximate solution to Equation (21) is

$$\widehat{\alpha}_{G_k} = \operatorname{hard}(\eta_{m_{G_k}}, \sqrt{2\tau}) = \eta_{m_{G_k}} \times 1[\operatorname{abs}(\eta_{m_{G_k}}) - \sqrt{2\tau}] \tag{23}$$

where $\operatorname{hard}(\cdot)$ denotes the hard thresholding operator. $1[\operatorname{abs}(\eta_{m_{G_k}}) - \sqrt{2\tau}]$ is defined as follows:

$$1[\operatorname{abs}(\eta_{m_{G_k}}) - \sqrt{2\tau}] = \begin{cases} 1, & \operatorname{abs}(\eta_{m_{G_k}}) > \sqrt{2\tau} \\ 0, & \operatorname{abs}(\eta_{m_{G_k}}) \leq \sqrt{2\tau} \end{cases} \tag{24}$$

The overall process of the SART-GSR algorithm is shown in Figure 4.

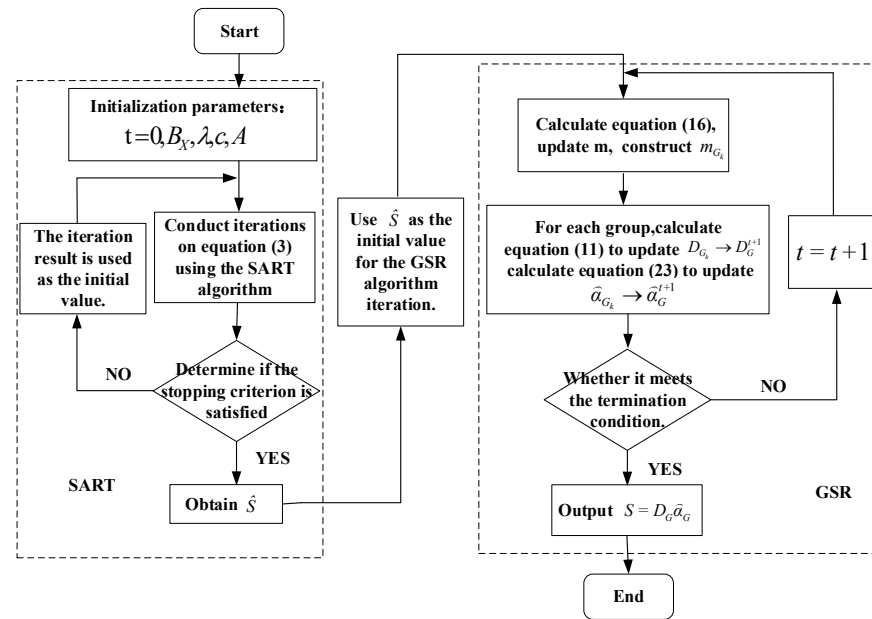


Figure 4. Flowchart of the SART-GSR algorithm.

5. Algorithm Verification and Result Evaluation

5.1. Algorithm Verification

To verify the feasibility and effectiveness of the established algorithm, a numerical simulation was conducted by employing concrete as a homogeneous medium model. Both low-speed and high-speed anomaly areas were set up within the model. A self-developed program was used to perform theoretical numerical calculations on the established medium model, and the results were analyzed to validate the feasibility and accuracy of the algorithm.

To study the impact of defects in different regions on the computed tomography imaging results, three defect conditions were designed. The medium model designed for this numerical simulation is shown in Figure 5, with dimensions of 30 m by 24 m. The grid is divided into 24 rows and 30 columns, totaling 720 cells, each measuring 1 m by 1 m.

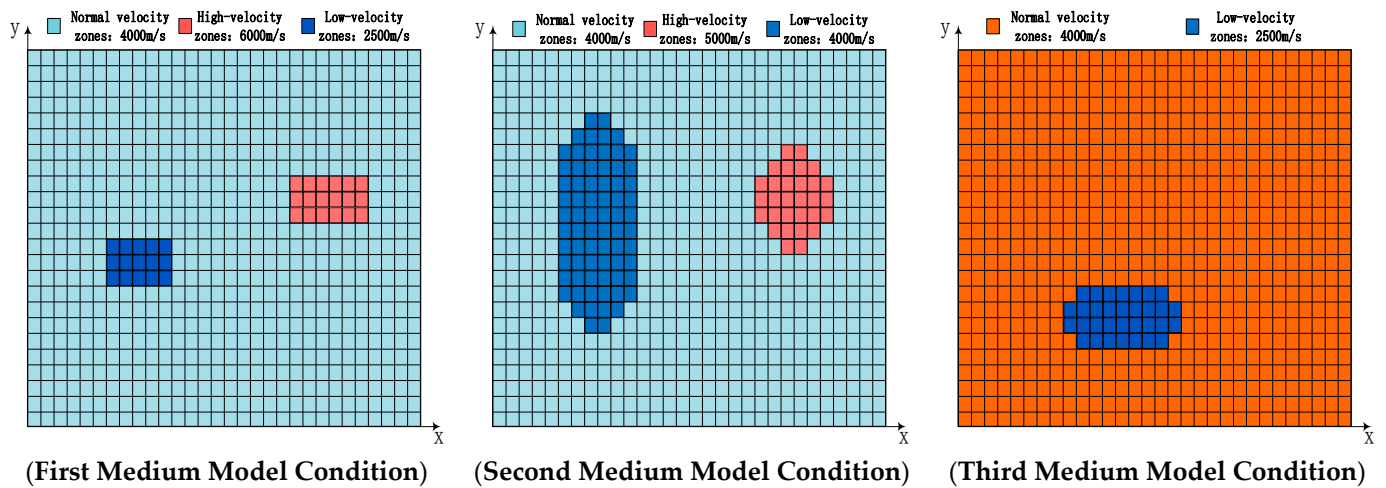


Figure 5. Medium model conditions.

The parameters for the GSR-SART algorithm were set as follows: $\lambda = 1$, with a block size of 4×4 , meaning $B_x = 16$, and the number of similar blocks $c = 9$. The measurement scheme for the concrete medium model involves placing measurement points (the green dots in the figure) on the upper and lower edges of the component, with excitation sources (the red dots in the figure) arranged in two central columns, thereby achieving a double-through coverage result for the area being tested. There are 11 measurement points on each side and 10 excitation points on each side of the middle part, totaling $2 \times 11 \times 20 = 440$ ray paths, as shown in Figure 6.

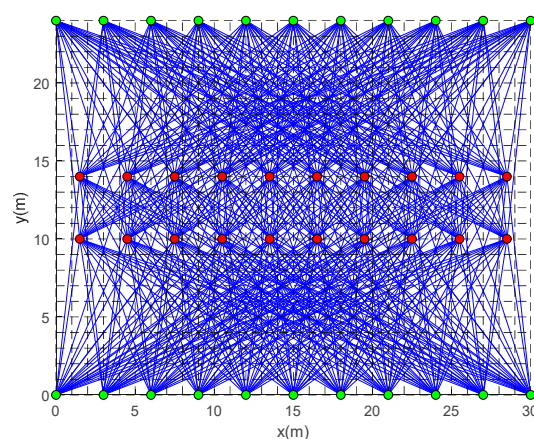


Figure 6. Media simulation ray paths.

To more intuitively compare the imaging effects and accuracy of the iterative reconstruction algorithms, namely, the ART, SART, and SART-GSR, these three algorithms were employed to perform inverse imaging of the aforementioned concrete medium wave velocity model. In order to smooth the wave velocity values of adjacent grids, the reconstruction results were processed with smoothing. The original number of grids was expanded one hundred times, and the wave velocity data were interpolated within two-dimensional data [25], making the tomographic imaging results more reasonable. The imaging results are shown in Figures 7–9.

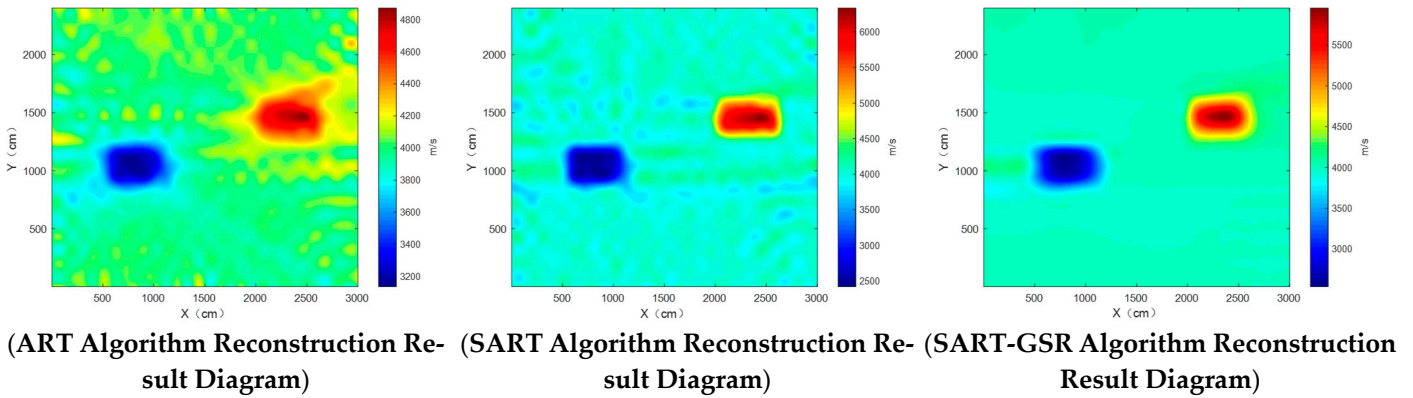


Figure 7. Medium model condition 1 algorithm reconstruction effect diagram.

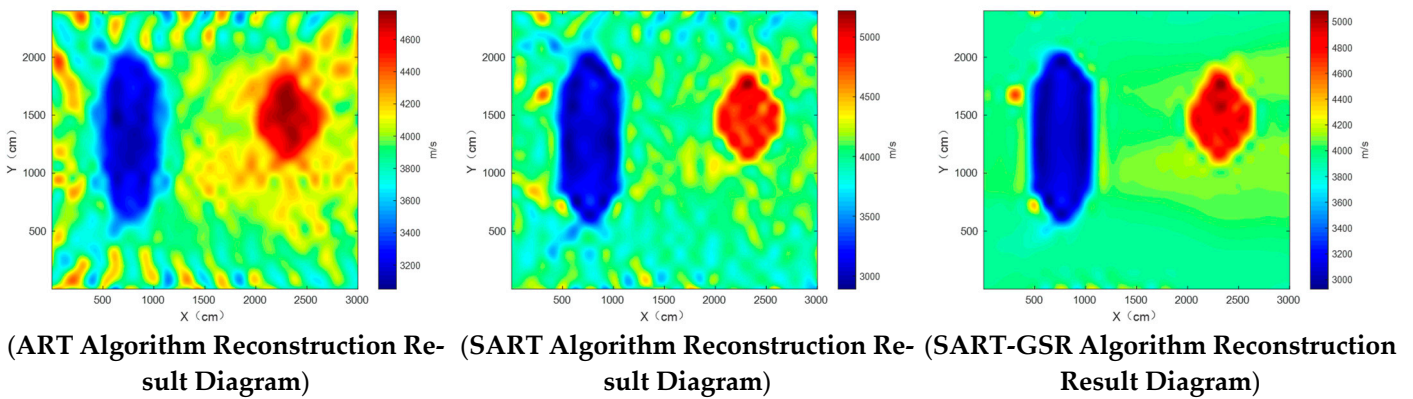


Figure 8. Medium model condition 2 algorithm reconstruction effect diagram.

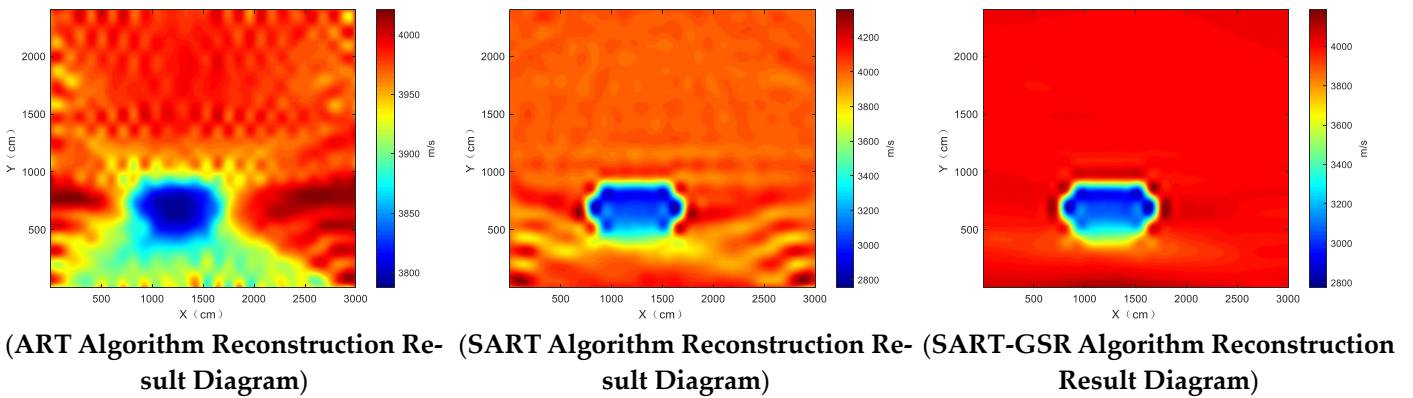


Figure 9. Medium model condition 3 algorithm reconstruction effect diagram.

By comparing the reconstruction results yielded by the three algorithms, it is evident that there are significant differences in the reconstruction effects around the defect areas. The ART algorithm produces relatively blurry imaging effects at the edges of abnormal wave velocity areas, whereas the SART and SART-GSR algorithms yield better reconstruction effects near the defect areas. By comparing Figures 5–7, it can be seen that the reconstructed image obtained via the SART is affected by internal noise, while the overall reconstruction effect of the SART-GSR algorithm is superior, with a more complete internal structure, showing a particularly clear advantage in the reconstruction results of non-abnormal areas. In summary, this algorithm offers better reconstruction effects than other reconstruction algorithms.

5.2. Field Experiment

To further compare the reconstruction effects of the three algorithms, a field experiment was designed for additional validation. This experiment involved casting concrete specimens with dimensions of 300 mm × 300 mm × 20 mm. The grid was divided into 30 × 30 sections, resulting in a total of 900 grid cells, each measuring 1 dm × 1 dm. The measurement scheme for the specimens was consistent with the simulation experiments, involving the placement of sensors on the edges of the top and bottom sides of the component, with excitation sources arranged in the two central columns, as shown in Figure 10. The layout of the field experiment is shown in Figures 11 and 12.

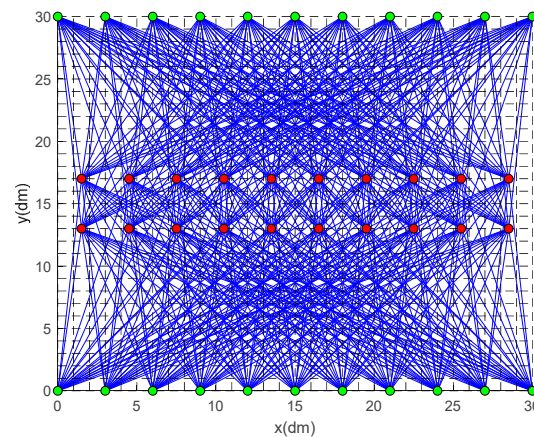


Figure 10. Field Experiment Medium simulation ray paths.



Figure 11. Partial Layout Diagram of Sensors in the Field Experiment.



Figure 12. Diagram of the entire layout of the sensors in the field experiment.

In order to more accurately verify the effects of three reconstruction algorithms and reduce the influence of random errors on the results, a measurement repeatability experiment was carried out: under the condition of ensuring the same measurement conditions, multiple repeated measurement experiments were conducted, and finally the average values of multiple measurements were used as experimental data for analysis. The imaging

results are shown in Figure 13. Comparing the reconstruction effects of the three algorithms reveals that the ART and SART algorithms are severely affected by noise interference. The SART-GSR algorithm effectively reduces the noise interference from the field experiment environment, resulting in an overall better reconstruction effect.

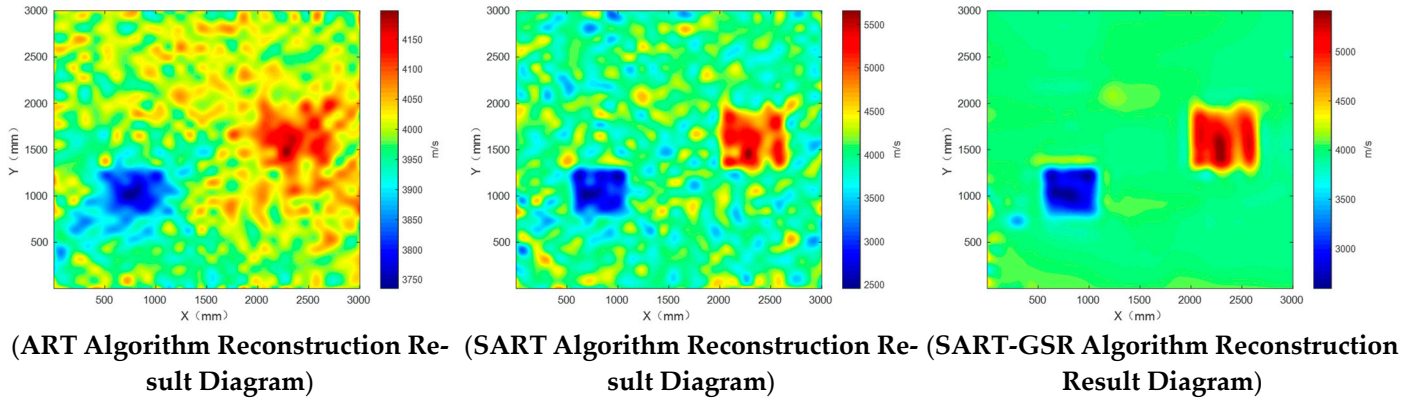


Figure 13. Diagram of the algorithm reconstruction effect in the field experiment.

5.3. Evaluation of Reconstruction Effects

In scientific research and engineering applications, the accuracy of algorithms directly affects the reliability and application value of the final results. To objectively evaluate the performance of the three algorithms in terms of reconstruction accuracy in the region of interest, we utilize two main error parameters, relative error (RE) and root mean square error (RMSE), to measure the reconstruction effects of different methods. The RE was primarily used to assess how closely each of the three methods' actual reconstruction effects for each grid within the wave velocity reconstruction area match the initial velocity model of the concrete medium. This parameter objectively reflects the accuracy of the reconstructed velocity model. Meanwhile, the RMSE was used to evaluate the deviation between the reconstruction results of the different algorithms across the entire area and the initially established medium model. The smaller its value, the closer the reconstruction results are to the initially set values, indicating better reconstruction effects. Overall, the RE and RMSE provide objective criteria for evaluating the accuracy of the different reconstruction methods from local and global perspectives, respectively. The equations for calculating the RE and RMSE are shown in Equations (25) and (26), respectively.

$$E_{RE} = \frac{|y_j - \hat{y}_j|}{\hat{y}_j} \times 100\% \tag{25}$$

$$E_{RMSE} = \sqrt{\frac{1}{J} \sum_{j=1}^J (y_j - \hat{y}_j)^2} \tag{26}$$

In the formulae, J represents the total number of grids in the reconstructed wave velocity field area; y_j represents the reconstruction result of each reconstruction algorithm in the j -th grid; and \hat{y}_j represents the theoretical true value in the j -th grid.

The Figure 14 shows the relative errors of the wave velocity values reconstructed by the ART, SART, and SART-GSR algorithms compared to the set wave velocity values in 720 grids within the reconstruction area. In the relative error graph, it can be seen that within the reconstruction area, the relative errors of the ART and SART algorithms are higher, and the relative error in some individual grids far exceeds the average error. This is due to reasons such as sparse ray coverage, which leads to some pixels in the reconstruction area not being correctly updated during the iteration process, especially at the edges of the image, where this effect is more pronounced. Additionally, truncation of projection data can also cause large errors in individual data points in the reconstructed image. The

missing data from the truncated parts result in related areas of the image not being correctly updated. The relative errors of the SART and SART-GSR are significantly lower than those of the ART algorithm. Compared to the SART algorithm, SART-GSR has an overall lower relative error, and it effectively reduces the high relative errors in some grids. The relative error of the wave velocity data for each grid reconstructed by the SART-GSR algorithm was maintained at approximately 1.5%, which is about a 4% reduction compared to the ART algorithm and an approximately 1.5% reduction compared to the SART algorithm. Furthermore, we evaluated the root mean square error (RMSE), which was used as an indicator to measure the overall error after reconstruction. As shown in Figure 15, it represents the RMSE values of the three algorithms in five experiments. The average RMSE values of the three algorithms in five experiments are shown in Table 1.

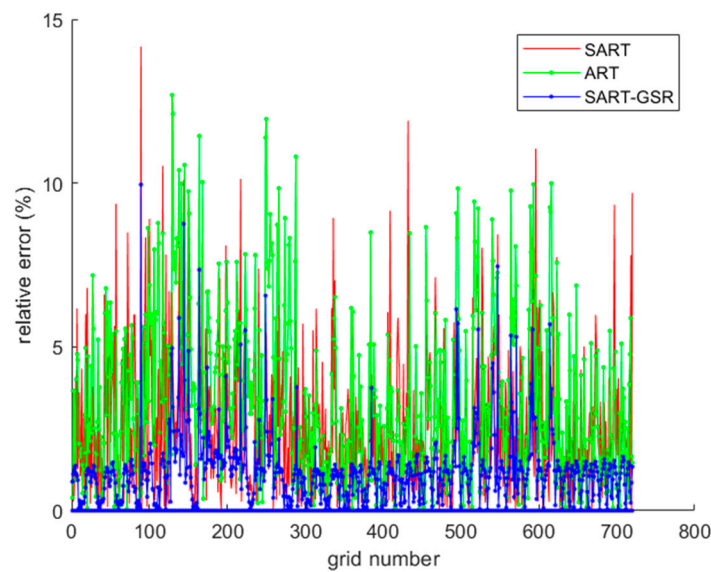


Figure 14. Relative error of velocity in each grid.

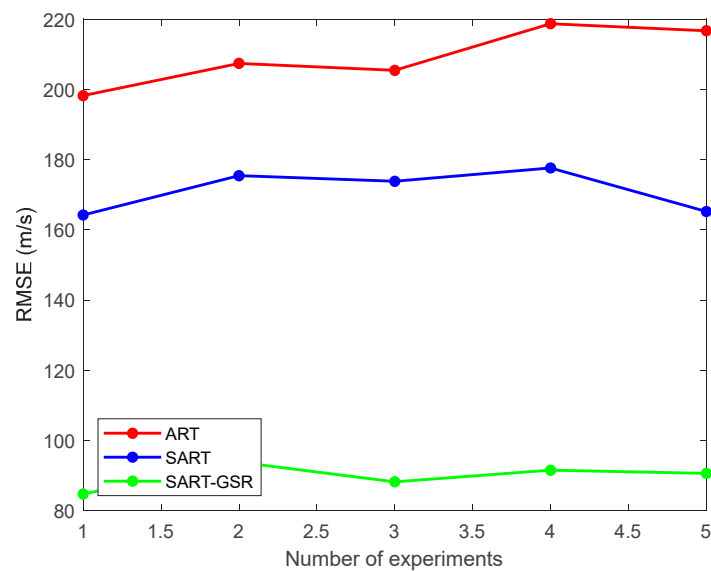


Figure 15. Comparison chart concerning the root mean square errors of the different algorithms.

Table 1. Comparison of reconstruction errors for different algorithms.

Reconstruction Algorithm	ART	SART	SART-GSR
RMSE (m/s)	209.28	171.24	89.76

In the table above, it can be seen that the root mean square errors (RMSEs) of the wave velocity reconstructions for the three different algorithms are 209.28 m/s, 171.24 m/s, and 89.76 m/s, respectively. From these two sets of error data, it is evident that the method proposed in this paper has a significantly lower overall wave velocity reconstruction error than the other two algorithms. By comprehensively analyzing both the relative error and the RMSE, it can be further directly demonstrated that the method proposed in this paper has more advantages in the reconstruction of bridge concrete wave velocities. Looking at the overall effect of data reconstruction, it is evident that the results obtained by the SART-GSR method have smaller errors than the simulated medium model, and the imaging error is significantly less than that of the ART and SART algorithms. Upon comprehensive analysis, in the practical development and application of wave velocity imaging for bridge concrete defect detection, among the three algorithms tested, the SART-GSR method achieves the best tomographic imaging results.

6. Conclusions

To further improve the precision of tomographic imaging for bridge concrete, this paper proposes a wave velocity inversion reconstruction method based on the SART-GSR algorithm. Through simulation experiments and comparison with traditional methods such as the ART and SART algorithms, the results show that the SART-GSR algorithm not only enhances the quality of the reconstructed image but also helps to preserve the edge information of the internal structure of the concrete. This allows for better identification and localization of defects, verifying the feasibility of the proposed method. It has significant implications for achieving rapid and efficient health monitoring and assessment of concrete structures and holds practical engineering value for the tomographic imaging of bridge concrete.

7. Discussion

The SART-GSR algorithm shows great potential in improving the accuracy and efficiency of health monitoring for concrete structures, with a wide range of application prospects. In dam maintenance, this technology is expected to provide high-resolution three-dimensional images useful for accurately identifying and locating defects, ensuring the structural safety of dams and thereby reducing the risk of catastrophic failure. Airport runway safety monitoring could also benefit from this technology; regular inspections can allow the timely detection and repair of problem areas, ensuring runway smoothness. In the field of historical-building preservation, internal inspections can be conducted without damaging the original structure, allowing for the timely detection and addressal of issues. The monitoring of underground pipelines and tunnels has also become more efficient, helping to prevent accidents. Additionally, this technology is promising for the remote monitoring of offshore platforms and oil-drilling platforms, reducing personnel risk and enhancing safety. These applications demonstrate the significant value and potential of the SART-GSR algorithm across various infrastructures and industrial sectors.

Author Contributions: Conceptualization, J.L. (Jian Li), J.L. (Jin Li), C.G., R.L. and L.W.; methodology, J.L. (Jian Li), J.L. (Jin Li) and H.W.; investigation, C.L., R.L. and L.W.; writing, J.L. (Jian Li) and J.L. (Jin Li). All authors have read and agreed to the published version of the manuscript.

Funding: This research was partly funded by the National Science Foundation of China General Program (No. 62271453), the National Natural Science Foundation of China (No. 62101512), Central Support for Local Projects (No. YDZJSX2024D031), the Shanxi Province Young Academic Leaders

Project (No. 2024Q022), and the Shanxi Province Patent Conversion Special Plan Funding Projects (No. 202405004).

Institutional Review Board Statement: Not applicable.

Informed Consent Statement: Not applicable.

Data Availability Statement: The data presented in this study are available on request from the corresponding author.

Conflicts of Interest: Author Hongtao Wu was employed by the company Shanxi Intelligent Transportation Laboratory Co., Ltd. The remaining authors declare that the research was conducted in the absence of any commercial or financial relationships that could be construed as a potential conflict of interest.

References

1. Karastathis, V.K.; Karmis, P.N.; Drakatos, G.; Stavrakakis, G. Assessment of the dynamic properties of highly saturated concrete using one-sided acoustic tomography, Application in the Marathon Dam. *Constr. Build. Mater.* **2002**, *16*, 261–269. [[CrossRef](#)]
2. Ravi Kumar, N.S.; Barkavi, T.; Natarajan, C. Structural health monitoring: Detection of concrete flaws using ultrasonic pulse velocity. *J. Build. Pathol. Rehabil.* **2018**, *3*, 6. [[CrossRef](#)]
3. Tatarinov, A.; Rumjancevs, A.; Mironovs, V. Assessment of cracks in pre-stressed concrete railway sleepers by ultrasonic testing. *Procedia Comput. Sci.* **2019**, *149*, 324–330. [[CrossRef](#)]
4. Zielińska, M.; Rucka, M. Detection of debonding in reinforced concrete beams using ultrasonic transmission tomography and hybrid ray tracing technique. *Constr. Build. Mater.* **2020**, *262*, 120104. [[CrossRef](#)]
5. Thiele, M.; Pirskawetz, S. Analysis of damage evolution in concrete under fatigue loading by acoustic emission and ultrasonic testing. *Materials* **2022**, *15*, 341. [[CrossRef](#)]
6. Donda, D.; Latosh, F.; Rahman, M.A.; Bagchi, A. Detection of subsurface defects in concrete slabs using ground penetrating radar. In *Nondestructive Characterization and Monitoring of Advanced Materials, Aerospace, Civil Infrastructure, and Transportation XV*; SPIE: Bellingham, WA, USA, 2021; Volume 11592, pp. 48–56.
7. Singh, S.K.; Narang, N.; Singh, D. Development of a novel approach to detect damage in concrete structures with millimeter wave radar assessment system. *Rev. Sci. Instrum.* **2021**, *92*, 044710. [[CrossRef](#)]
8. Ma, Y.; Elseifi, M.A.; Dhakal, N.; Bashar, M.Z.; Zhang, Z. Non-destructive detection of asphalt concrete stripping damage using ground penetrating radar. *Transp. Res. Rec.* **2021**, *2675*, 938–947. [[CrossRef](#)]
9. Jin, H.; Zou, L.L. Detection of hidden disease of concrete bridge based on infrared thermal imaging. *J. Phys. Conf. Ser.* **2021**, *1748*, 042041.
10. Goffin, B.; Banthia, N.; Yonemitsu, N. Use of infrared thermal imaging to detect corrosion of epoxy coated and uncoated rebar in concrete. *Constr. Build. Mater.* **2020**, *263*, 120162. [[CrossRef](#)]
11. Keo, S.A.; Szymanik, B.; Le Roy, C.; Brachelet, F.; Defer, D. Defect detection in CFRP concrete reinforcement using the microwave infrared thermography (MIRT) method—A Numerical Modeling and Experimental Approach. *Appl. Sci.* **2023**, *13*, 8393. [[CrossRef](#)]
12. Yaacob, M.L.M.; Idris, N.H.; Zainuddin, K.; Dollah, R.; Yusof, N.M.; Abd Rahaman, N.; Ahmad, S.; Hamid, N.A.; Mhapo, A.M. Bridge Pillar Defect Detection using Close Range Thermography Imagery. *Int. J. Adv. Comput. Sci. Appl.* **2022**, *13*, 599–606.
13. Scherr, J.F.; Grosse, C.U. Delamination detection on a concrete bridge deck using impact echo scanning. *Struct. Concr.* **2021**, *22*, 806–812. [[CrossRef](#)]
14. Liu, Y.L.; Liu, Z.; Lai, S.K.; Luo, L.Z.; Dai, J.G. Debonding detection in the grouted joints of precast concrete shear walls using impact-echo method. *J. Nondestruct. Eval.* **2021**, *40*, 50. [[CrossRef](#)]
15. Hu, X.; Wang, Y.; Zhang, G.; Du, L. Application of Impact Elastic Wave Method in Quality Inspection of Concrete Lining. *J. Phys. Conf. Ser.* **2023**, *2651*, 012079.
16. Hongyan, L.; Zhonglin, W. A modified algebraic reconstruction algorithm for sparse projection. *Ann. Transl. Med.* **2021**, *9*, 1422.
17. Ghanbari, S.; Woods, J.C.; Lucas, S.M. Semi-automatic BPT for image retrieval. In *Proceedings of the 2009 Seventh International Workshop on Content-Based Multimedia Indexing, Chania, Greece, 3–5 June 2009*; IEEE: Piscataway, NJ, USA, 2009; pp. 33–37.
18. Agarwal, C.; Mhatre, A.; Patra, S.; Chaudhury, S.; Goswami, A. Algebraic reconstruction technique combined with Monte Carlo method for weight matrix calculation in gamma ray transmission tomography. *SN Appl. Sci.* **2019**, *1*, 1157. [[CrossRef](#)]
19. Yan, M. Convergence analysis of SART: Optimization and statistics. *Int. J. Comput. Math.* **2013**, *90*, 30–47. [[CrossRef](#)]
20. Hu, Y.; Li, Y.; Liu, Y.; Qin, J. Theory and Algorithm of Structural Sparse Optimization Model. *Sci. China Math.* **2024**, *54*, 1045–1070.
21. Cai, L.; Feng, X.; Yu, H. Reinforcement Learning with Sparse Representation via Sparse Overlapping Group Lasso. *J. East China Univ. Sci. Technol.* **2024**.
22. Li, X.; Fu, H.; Song, B. Fluorescence Diffusion Optical Tomography Reconstruction Based on Group Sparsity Regularization. *Prog. Laser Optoelectron. Technol.* **2021**, *58*, 251–257.
23. Peng, B.; Zhou, J.; Zhang, Y. Few-view CT reconstruction with group-sparsity regularization. *Int. J. Numer. Methods Biomed. Eng.* **2018**, *34*, e3101.

24. Zhang, Q.; Zhang, J.; Lu, S.; Liu, Y.; Liu, L.; Wang, Y.; Cao, M. Multi-Resolution Feature Extraction and Fusion for Traditional Village Landscape Analysis in Remote Sensing Imagery. *Trait. Du Signal* **2023**, *40*, 1259. [[CrossRef](#)]
25. Li, J.; Ren, J.; Fan, X.; Zhou, P.; Pu, Y.; Zhang, F. Estimation of unfrozen water content in frozen soils based on data interpolation and constrained monotonic neural network. *Cold Reg. Sci. Technol.* **2024**, *218*, 104094. [[CrossRef](#)]

Disclaimer/Publisher's Note: The statements, opinions and data contained in all publications are solely those of the individual author(s) and contributor(s) and not of MDPI and/or the editor(s). MDPI and/or the editor(s) disclaim responsibility for any injury to people or property resulting from any ideas, methods, instructions or products referred to in the content.